




## Article

# Fabrication of Carbon/Zinc Oxide Nanocomposites as Highly Efficient Catalytic Materials for Application in Dye-Sensitized Solar Cells

Hussain Gulab <sup>1,\*</sup>, Nusrat Fatima <sup>1</sup>, Nadia Shahzad <sup>2</sup> , Muhammad Imran Shahzad <sup>3</sup> , Mohsin Siddique <sup>1,4</sup>, Muhammad Hussain <sup>5</sup> and Muhammad Humayun <sup>6,\*</sup> 

<sup>1</sup> Department of Chemistry, Bacha Khan University, Peshawar 24420, Pakistan

<sup>2</sup> US-Pakistan Centre for Advanced Studies in Energy (USPCAS-E), National University of Science and Technology (NUST), Islamabad 44000, Pakistan

<sup>3</sup> Nanosciences and Technology Department (NS & TD), National Centre for Physics (NCP), Islamabad 44000, Pakistan

<sup>4</sup> Department of Chemistry, University of Sialkot, Sialkot 51040, Pakistan

<sup>5</sup> Department of Physics, Bacha Khan University, Peshawar 24461, Pakistan

<sup>6</sup> Wuhan National Laboratory for Optoelectronics, School of Optical and Electronics Information, Huazhong University of Science and Technology, Wuhan 430074, China

\* Correspondence: hussaingulab@gmail.com (H.G.); 2017511018@hust.edu.cn (M.H.)



**Citation:** Gulab, H.; Fatima, N.; Shahzad, N.; Shahzad, M.I.; Siddique, M.; Hussain, M.; Humayun, M. Fabrication of Carbon/Zinc Oxide Nanocomposites as Highly Efficient Catalytic Materials for Application in Dye-Sensitized Solar Cells. *Catalysts* **2022**, *12*, 1354. <https://doi.org/10.3390/catal12111354>

Academic Editors: Ciro Bustillo-Lecompte, Mehrab Mehrvar, Lesly Tejeda-Benitez and Fiderman Machuca-Martínez

Received: 27 September 2022

Accepted: 20 October 2022

Published: 3 November 2022

**Publisher's Note:** MDPI stays neutral with regard to jurisdictional claims in published maps and institutional affiliations.



**Copyright:** © 2022 by the authors. Licensee MDPI, Basel, Switzerland. This article is an open access article distributed under the terms and conditions of the Creative Commons Attribution (CC BY) license (<https://creativecommons.org/licenses/by/4.0/>).

**Abstract:** Different nanostructured semiconducting ZnO photoanodes were prepared by Hydrothermal (HT), Co-precipitation (CoP) and Chemical Bath Deposition (CBD) methods for their use in the Dye Sensitized Solar Cells (DSSCs) in the present study. Additionally, different ZnO nanocomposites were synthesized by mixing the Carbon Nanotubes (CNTs), Graphene Oxide (GO) and their combination with the ZnO nanostructures. Scanning electron microscopy (SEM) revealed various morphologies of ZnO nanostructures and nanocomposites such as nanoflowers, nanorods, rhombohedral, cubic, and cauliflower-like nanorods, and nanorods with hexagonal symmetry. Energy Dispersive X-ray (EDX) spectra confirmed the purity of the synthesized samples. X-ray Diffraction (XRD) demonstrated the hexagonal wurtzite phase of ZnO and a minor presence of CNTs and graphene. The UV-Visible, transmittance and diffuse reflectance spectra demonstrated that the ZnO synthesized through the CBD method exhibits the highest transmittance as 70–71% in the UV-Vis range and reduced % R. Optical band gaps of the samples were determined with the help of Tauc plots. Comparison of J-V characteristics showed that the ZnO synthesized via the HT method exhibits the highest conversion efficiency of 1.45%. Comparison among pristine ZnO synthesized via CBD and ZnO nanocomposites revealed that ZnO/CNTs possesses the highest energy conversion efficiency of 1.23% with enhanced  $J_{SC}$  of 4.49 mA/cm<sup>2</sup>.

**Keywords:** ZnO; DSSCs; photoanodes; carbon nanomaterials; hydrothermal

## 1. Introduction

The swiftly growing utilization of fossil fuels and the discharge of greenhouse gases puts a noteworthy stress on global energy demands and has led to calls for environmental protection [1]. Solar energy is considered as the most promising and attractive renewable energy source. Solar energy in the form of a carbon-neutral energy resource is one of the leading answers to various challenges concerning energy and the environment. After the origination of the photovoltaic effect by a French physicist Alexander Edmond Becquerel in the year 1839 [2], the struggles for direct transformation of sunlight into electricity have undergone remarkable developments. Solar cells show tremendous advantages over other energy technologies, and they include lack of transmission losses, need little continuation and maintenance, nontoxicity and noiseless working enjoyment [3].

Brian O'Regan and Michael Gratzel were the first to present the idea of these -sensitizer-based solar cells in 1991 [4]. Research studies have been increasingly growing for the efficient enhancement and improved stability of dye-sensitized solar cells (DSSCs) by elevating the performance of their constituents. Reduced efficiency, expensive conducting substrates, ruthenium dyes and platinum are few flaws of DSSCs which need to be improved. Photoanodes are one of the vital and basic DSSC components due to their function in scaffolding dye molecules and their assistance in photogenerated electrons transportation towards external circuits [5]. These porous nanocrystalline semiconductor oxide films have a sufficient surface area for dye loading which performs the important task of converting of photons into electrical energy. For better performance, a photoanode must retain a large surface area, efficient electron transport properties and a low electron-hole recombination rate [6,7].

Numerous approaches have been suggested for the selection of an ideal photoanode [8]. Various inorganic semiconducting oxides such as  $\text{TiO}_2$ ,  $\text{ZnO}$ ,  $\text{Zn}_2\text{SnO}_4$ ,  $\text{Nb}_2\text{O}_5$ ,  $\text{WO}_3$ ,  $\text{SnO}_2$ ,  $\text{Fe}_2\text{O}_3$ ,  $\text{SrTiO}_3$ ,  $\text{ZrO}_2$ ,  $\text{Al}_2\text{O}_3$ ,  $\text{CeO}_2$  and carbon nanomaterials are employed to work as photoanodes with the band gap almost equal to the sensitizer optical band to aid in the effective injection of excited electron [9]. Among all these materials,  $\text{TiO}_2$  and  $\text{ZnO}$  are argued to be favorable crucial photoanodes, most probably due to their better porosity and higher electronic mobility which facilitates greater adsorption of organic sensitizers [10,11].  $\text{ZnO}$  is a cost-effective material which can be obtained easily with variations in its morphology as well as production [12]. Moreover, besides variety of its features, the diversity in  $\text{ZnO}$  synthesis techniques offers further new multiplicities for efficiency enhancement [13–16]. Structural and morphological variations of the photoanodes can have a significant effect on PCE due to direct relation to the dye adsorption and charge transport. The  $\text{ZnO}$  nanomaterials have a variety of one dimensional (1D), two-dimensional (2D) and three-dimensional (3D) structures and morphologies, which make them a building block for various optoelectronic devices. One-dimensional structural forms includes nanorods [17,18], nanobelts [19,20], needles [21,22], nanowhiskers [23,24], nanorings [20], nanosprings and nanohelices [19], nanocages [25], nanopores [26], nanotetrapods [27], nanopropeller [28], nanowires [29], nanobows [30], nanopoints [31], nanobridge and nanonails [32], nanocombs [33], nanotips [34], nanodisks [35], nanotubes [36], etc. Nanopellets and nanosheets [37] are 2D structures, while the 3D structure of  $\text{ZnO}$  includes nanoflower [38], nanoflakes [39] and dandelion [40,41].

The proposed research work is aimed at growing morphologically different  $\text{ZnO}$  nanostructures through easy, inexpensive and environmentally-friendly wet chemical techniques by varying the growth conditions as they have the capability to improve the electron transport properties significantly. These wet chemical techniques include chemical bath deposition (CBD), hydrothermal and co-precipitation techniques. The growth conditions for the  $\text{ZnO}$  nanorods have been optimized. Then, the nanostructured composites have been fabricated by incorporating the carbon nanomaterials, i.e., graphene and CNTs, into  $\text{ZnO}$  nanostructures to present highly efficient and pure light harvesting strategies for electron transport enhancement in the photovoltaic (PV) devices. A novelty of the present work is that the cauliflower-like nanorods of carbon/Zinc oxide nanocomposites have never been reported in the literature for their application as catalysts in dye-sensitized solar cells.

## 2. Results and Discussion

### 2.1. X-ray Diffraction (XRD) Analysis

The XRD analyses of all the nanostructures and nanocomposites prepared through different techniques of HT, CBD and CoP were carried out for understanding the geometry of the synthesized crystalline materials.

### 2.1.1. XRD Analysis of ZnO Nanostructures

The XRD patterns of all the three ZnO nanostructures grown by different methods are given in Figure 1. All the three ZnO nanostructures demonstrated diffraction peaks at  $2\theta = 31.6^\circ, 34.5^\circ, 36.3^\circ, 47.3^\circ, 56.6^\circ, 62.8^\circ, 67.8^\circ, 68.1^\circ$ , and  $69.2^\circ$  which correspond to the (100), (002), (101), (102), (110), (103), (200), (112), and (201) planes, respectively. All these peaks are recognized and correspond to the standard hexagonal wurtzite structure of crystalline ZnO. The most prominent and sharp peak is at (101) (100), which indicates that all the synthesized samples are good crystalline materials. Furthermore, no extra peaks were observed that can be related to any impurity or transitional material, which indicates the purity of the grown ZnO nanomaterial.

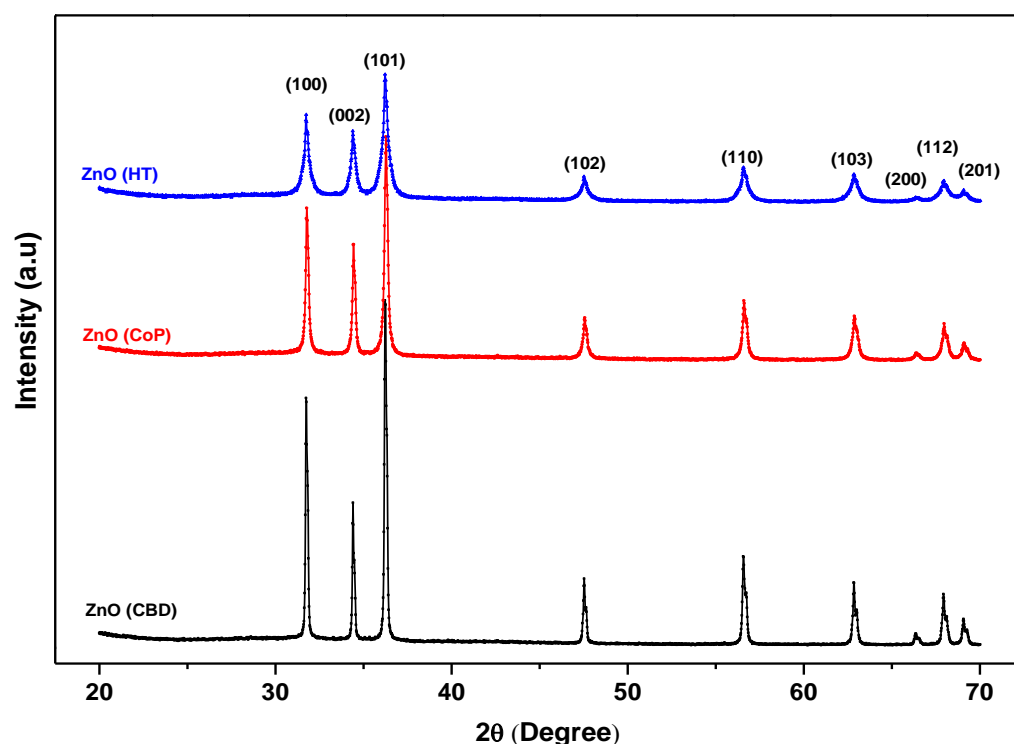


**Figure 1.** XRD pattern of ZnO nanostructures obtained via the HT, CoP and CBD methods.

It has already been demonstrated that the ZnO nanomaterials have a variety of one-dimensional (1D) [17–22], two-dimensional (2D) [37], and three-dimensional (3D) structures [38–41] and morphologies, which make them a building block for various optoelectronic devices.

### 2.1.2. XRD Analysis of ZnO/CNTs/GO Nanocomposites

The XRD patterns of ZnO/GO, ZnO/CNTs, and ZnO/CNTs + GO nanocomposites are shown in Figure 2. All the characteristic peaks of the wurtzite structure of ZnO are visible in the XRD diffractogram. Since the GO (0.05 wt.%) and the MWCNTs (0.05 wt.%) have been taken in very small proportions, the graphene and MWCNTs concentration ratio with respect to ZnO was very low, thus observable diffraction peaks could not be recorded in the XRD spectra. However, in the case of the ZnO/CNTs sample, the characteristic peak of GO at  $2\theta = 25^\circ$  was not identified in the diffractogram.

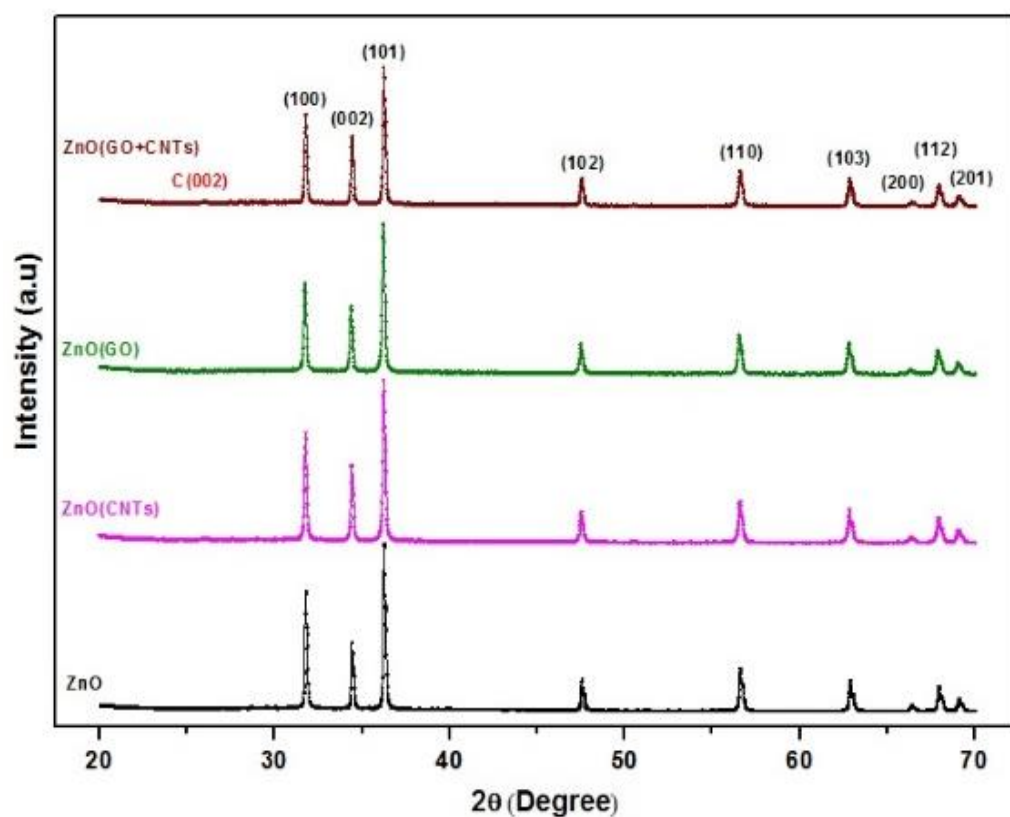


**Figure 2.** XRD pattern of the ZnO, ZnO (CNTs), ZnO (GO) and ZnO/CNTs/GO samples.

The crystallite size ( $D$ ) of the samples is estimated using the Scherrer formula:

$$D = \frac{K\lambda}{\beta 2\theta \cos \theta} \quad (1)$$

where  $k$  is a constant taken to be 0.94,  $\lambda$  is the wavelength of the X-ray used ( $\lambda = 1.54 \text{ \AA}$ ) and  $\beta 2\theta$  is the full width at half maximum (peak width) of (101) peak of the XRD pattern, Bragg angle is  $2\theta$  value of sharp peak. The crystallite size values given in Table 1 show that the ZnO synthesized via CBD exhibited the largest crystalline size of 51.37 nm and the ZnO prepared by the HT process revealed a reduced crystalline size of 17.47 nm. Moreover, among the nanocomposites, the ZnO/GO revealed a small crystal size of 45.96 nm. The XRD analysis revealed that all of the samples could be perfectly indexed as hexagonal wurtzite structures for ZnO (JCPDS NO. 36-1451) without any impurity phases. Furthermore, their diffraction peaks were sharp and intense, indicating that the ZnO nanostructures were highly crystalline.

**Table 1.** Crystallite size of nanostructures and nanocomposites.

Samples	Peak Width (FWHM)	Peak Position ( $2\theta$ )	Crystallite Size (nm)
ZnO (CBD)	0.17	36.2	~51.37
ZnO (CoP)	0.24	36.2	~36.39
ZnO (HT)	0.50	36.2	~17.47
ZnO (CNTs)	0.18	36.2	~48.51
ZnO(GO)	0.19	36.2	~45.96
ZnO (CNTs + GO)	0.18	36.2	~48.51

## 2.2. Optical Analysis

The synthesized nanostructures and nanocomposites were optically characterized and their diffuse reflectance and optical transmittance were recorded in order to investigate the optical behavior and band gap of the synthesized nanomaterial.

### 2.2.1. Optical Analysis of ZnO Nanostructures

The diffuse reflectance and optical transmittance spectra of Zinc Oxide nanostructures synthesized by various techniques are given in Figure 3. A, B. Sinusoidal transmittance spectra have been exhibited by the Zinc Oxide films in the visible region because of their layered structure. Highest percent transmittance (T%) up to 71% can be observed in the case of ZnO synthesized by the CBD method with an absorption edge at 380 nm in the UV–Vis range. The ZnO synthesized by the HT and CoP methods revealed an average T% of about 41% with an absorption edge at 379 nm, and 31% with an absorption edge at 378 nm, respectively. Thus, a blue shift can be observed as we move from CBD to the HT method and then to the CoP method. The ZnO film synthesized by the CBD method exhibiting the highest T% is attributed to the large crystallite size of the film. Furthermore, the reduction in T% is correlated to light scattering because of grain boundaries. The lowest T% of ZnO nanostructure synthesized by the CoP method caused an increment in the percent reflectance (R%) as demonstrated by the diffuse reflectance spectra, and thus the highest R% of about 69.9% was recorded for this sample. On the other hand, the ZnO synthesized by the CBD method exhibiting the highest transmittance showed a decreased R% of about 24.12%. Moreover, the ZnO synthesized by the HT method showed a 68% reflectance. All these variations can be correlated to the difference in light scattering caused by the crystallite size.

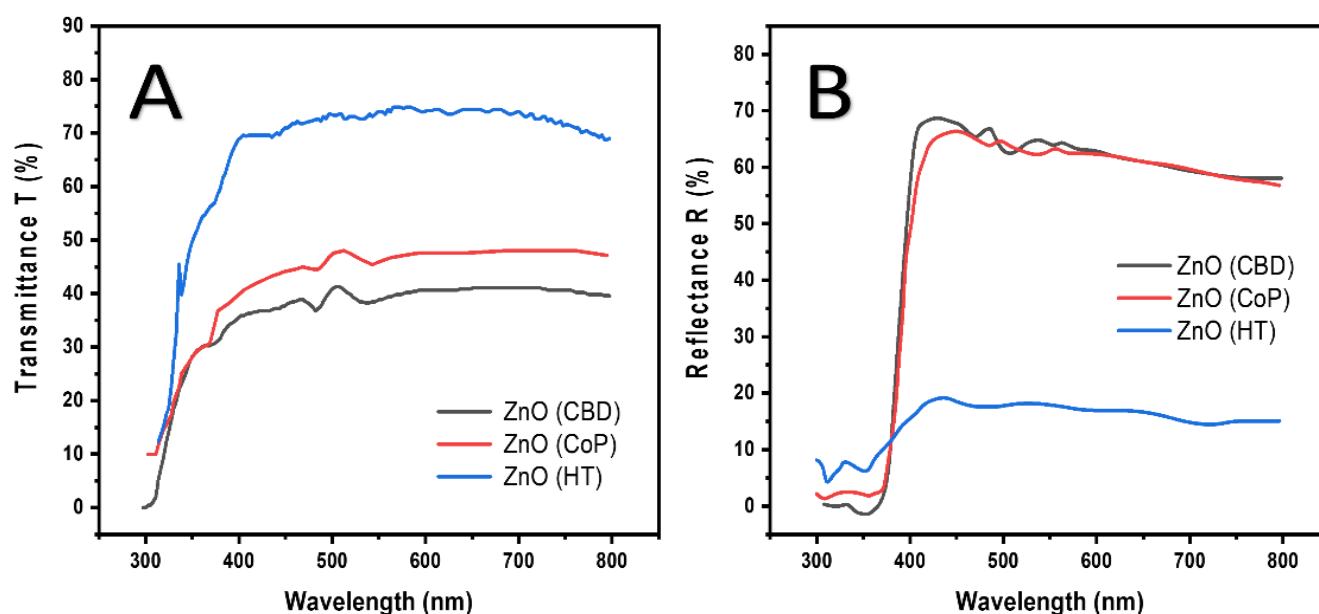


**Figure 3.** (A) Percent Transmittance (T%) and (B) Percent Reflectance (R%) spectra of ZnO grown by various techniques.

### 2.2.2. Optical Analysis of ZnO/CNTs/GO Nanocomposites

The T% and R% of the pure ZnO nanostructure and its nanocomposites with carbon have been compared and displayed in Figure 4 A,B. It reveals that the pristine ZnO exhibited the highest transmittance at around 71% with an absorption edge at 380 nm. The ZnO nanocomposite with CNTs shows a lower value of T% (30%) having the absorption edge at 369 nm. The ZnO nanocomposite with GO shows a T% of about 25% and the absorption edge can be observed at 372 nm. The ZnO nanocomposite with CNTs and GO demonstrated the lowest T% of about 20.12% with an absorption edge at 370 nm.

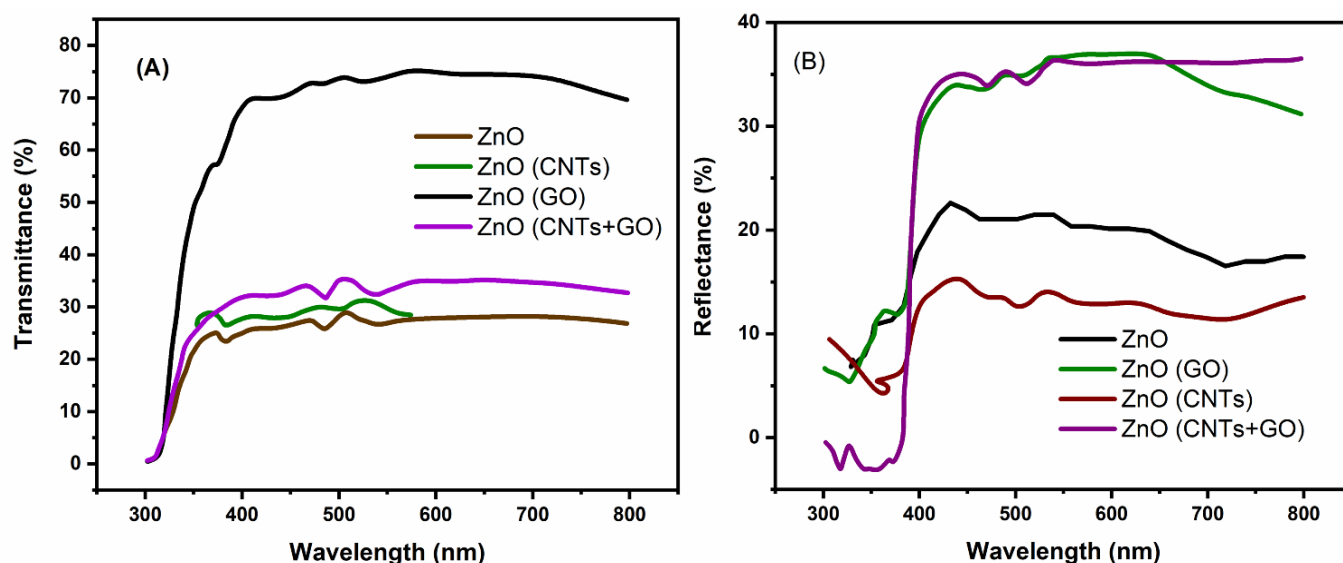


Figure 4. (A) Transmittance (T%), and (B) Reflectance (R%), spectra of Carbon/ZnO nanocomposites.

Diffuse reflectance spectra reveal that the pure ZnO with the highest T% values exhibit the lower reflectance, i.e., 24.12%. The ZnO nanocomposites with CNTs which have a lower T% show the highest reflectance of 34.20% and an absorption edge at 369 nm. The ZnO/GO showed reflectance of 35% with an absorption edge at 372 nm. The ZnO/CNTs/GO revealed the lowest reflectance of 19% with an absorption edge at 380 nm and showed an enhanced absorption. The shifting of absorption edges towards the higher wavelength indicates the reduction in optical band gaps value of the nanocomposites analyzed by the Tauc plots.

### 2.3. Band Gap Calculations

The optical band gaps of the synthesized samples were calculated by using the Tauc relation given as:

$$\alpha(\nu) = A \frac{(h\nu - E_g)^n}{h\nu} \quad (2)$$

where  $\alpha$  is the optical absorption coefficient,  $A$  is the proportionality constant,  $h\nu$  is the incident photons energy,  $\nu$  is the frequency and  $n$  is the exponent whose value depends on the transition type, i.e.,  $1/2$  for the allowed direct transition,  $2$  for the allowed indirect transition.  $3/2$  relates to the forbidden direct transition and  $3$  corresponds to the forbidden indirect transition. The ZnO shows the allowed direct transition corresponding to  $n = 1/2$ . Absorption coefficient ( $\alpha$ ) is related to the strong absorption peak of the synthesized samples and depends on absorbance ( $A$ ) and the thickness ( $t$ ) of the sample, i.e., the band gap is determined by plotting a curve between  $(h\nu)$  and  $(F(R)h\nu)^{1/2}$  and extrapolating the curve linear portion to  $(F(R)h\nu)^{1/2} = 0$ .

$$\alpha = 2.303A/t \quad (3)$$

The deviation of  $(F(R)h\nu)^{1/2}$  on the y-axis versus  $h\nu$  on the x-axis for ZnO nanostructure and carbon/ZnO composites synthesized via CBD are shown in Figure 5, and the measured values are illustrated in Table 2.

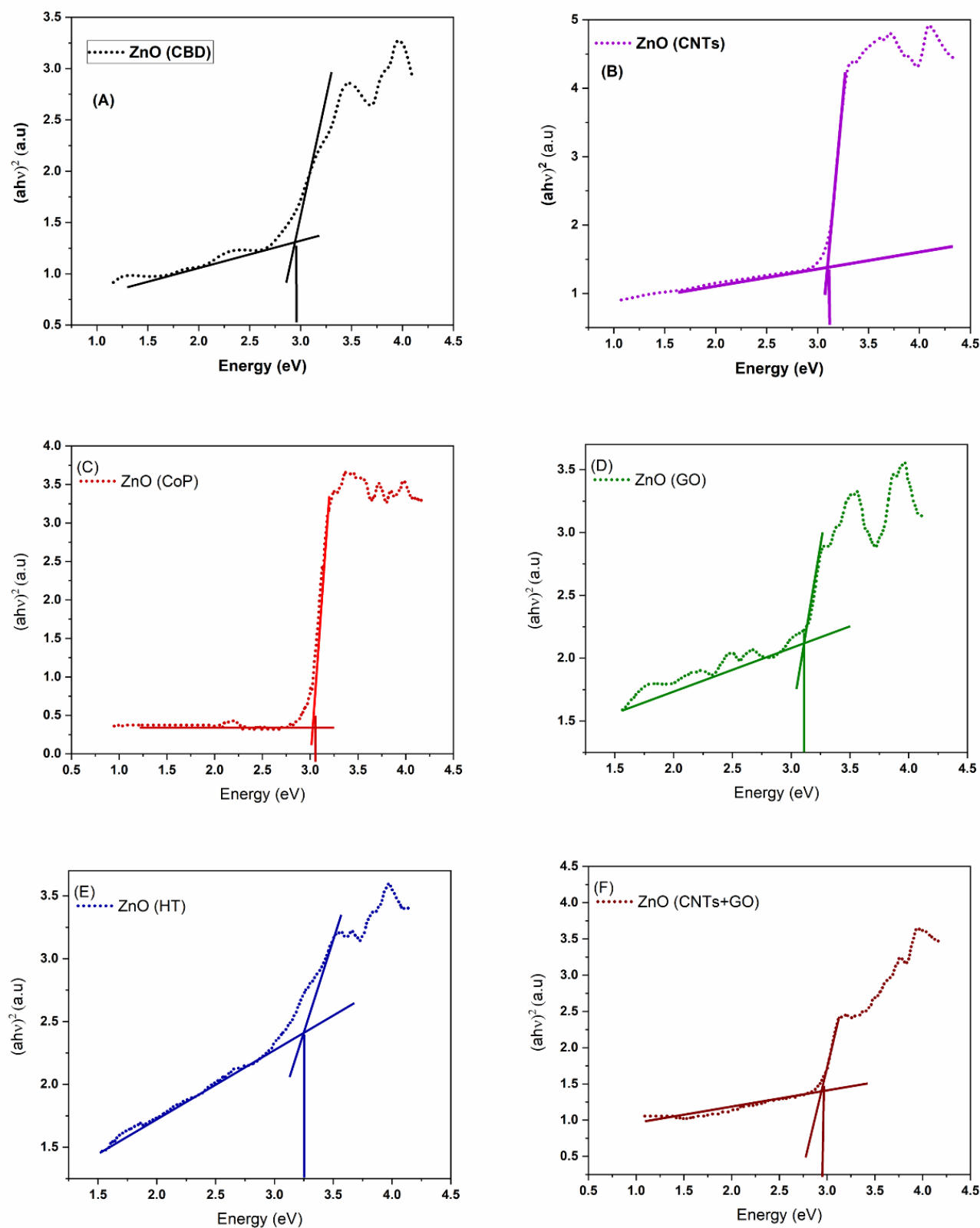


**Figure 5.** Tauc plots for band gap calculation of ZnO ((A)—CBD, (B)—CNTs, (C)—CoPs, (D)—GO, (E)—HT, and (F)—CNTs + GO) nanostructures and composites.

**Table 2.** Band gaps for the ZnO nanostructures and carbon/ZnO nanocomposites.

Samples	Band Gap Values Using F(R) Spectra		Band Gap Values Using T and R Spectra	
	Band Gap (eV)	Error (eV)	Band Gap (eV)	Error (eV)
ZnO (CBD)	3.15	±0.05	3.20	±0.08
ZnO (CoP)	3.20	±0.05	3.20	±0.08
ZnO (HT)	3.21	±0.05	3.21	±0.08
ZnO/CNTs	3.20	±0.05	3.19	±0.08
ZnO/GO	3.19	±0.05	3.18	±0.08
ZnO/CNTs/GO	3.18	±0.05	3.19	±0.08

Similarly, the optical band gap can also be determined with the help of the Transmittance and Reflectance spectra of the synthesized samples. By using R and T spectra, and by knowing the film thickness ( $d$ ), the absorption coefficient ( $\alpha$ ) can be calculated by the following equation:

$$\alpha = \frac{1}{d} \ln \left( \frac{1-R}{T} \right) \quad (4)$$

The optical band gap ( $E_g$ ) of ZnO can be correlated to absorption coefficient ( $\alpha$ ) by using equation:

$$\alpha h\nu = \text{const} (h\nu - E_g)^{1/2} \quad (5)$$

Plotting the curve between  $(\alpha h\nu)^2$  versus photon energy ( $h\nu$ ), the optical band gap values are recorded by extrapolating the straight lines to zero (Figure 6). The calculated values are illustrated in Table 2. The measured values have a possible error of  $\pm 0.08$  eV, which is correlated to the spectrophotometric measurements besides the curve extrapolation.

## 2.4. Morphology of ZnO Nanostructures

### 2.4.1. Morphology of ZnO Nanostructures Grown via the Hydrothermal Method

ZnO nanostructures were grown by means of a hydrothermal technique (HT) at 120 °C for 12 h in an autoclave directly on the FTO substrate achieving a 12  $\mu\text{m}$  thickness. The planned growth yielded small sized nanoflowers (NFs), which show potential to act as effective photoanode in a DSC. Surface morphology of the film plays a vital role in investigation of its microstructure. The SEM images of the ZnO film at different magnifications has been presented in Figure 7A–F, which show nanoflower morphology having some nanoflakes on the surface. The average thickness of the flakes is observed to be about 53.02 nm. The literature reveals that ZnO nanomaterials have various structures, i.e., one-dimensional (1D), two-dimensional (2D), and three-dimensional (3D) structures and morphologies, which enable them to be a building block for various optoelectronic devices [36–38]. It has been demonstrated that the arbitrary branches of the nanoflowers film offer a high specific surface area and greater contact among light and dye besides retaining high electronic transport [38].

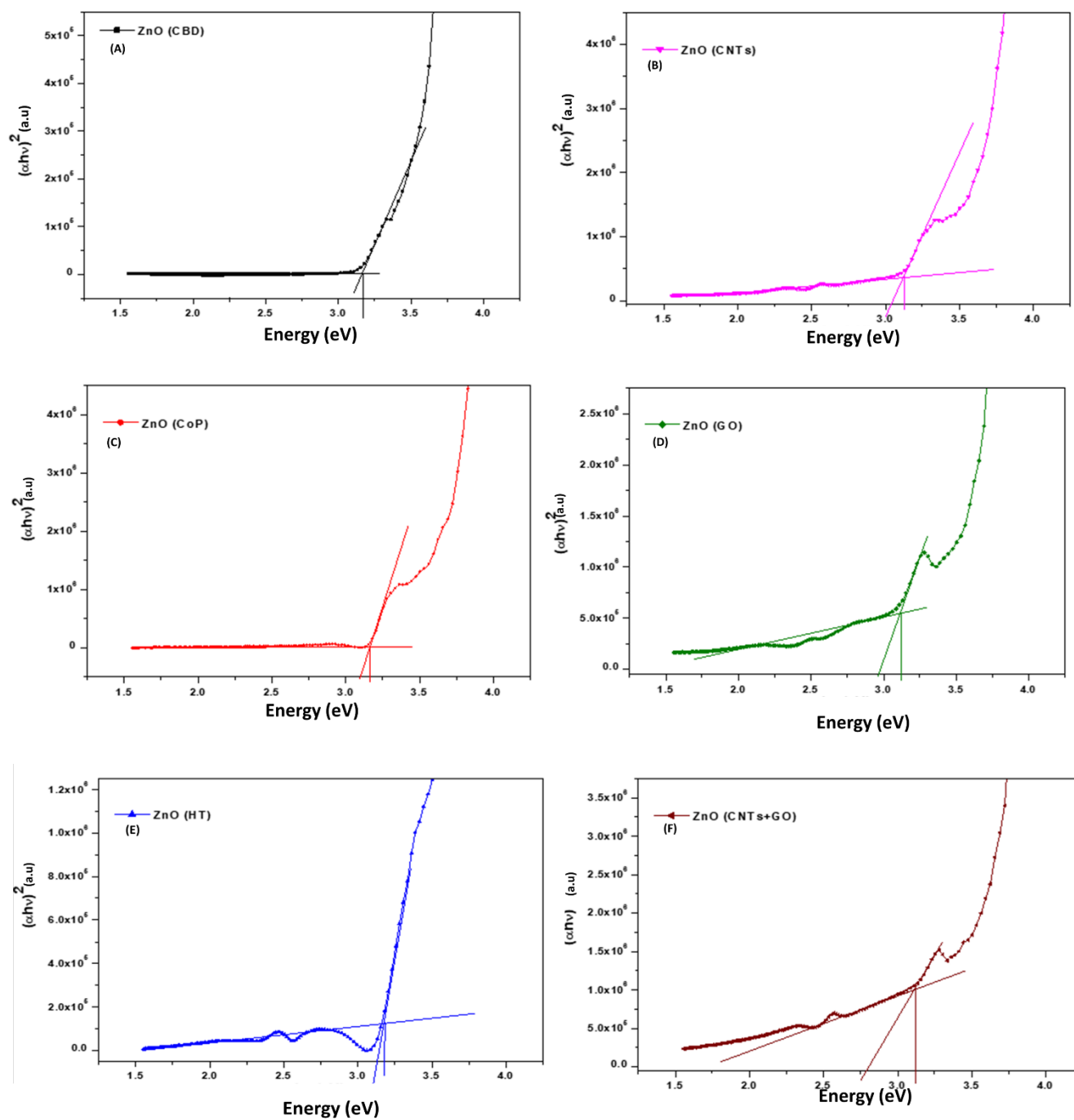


**Figure 6.** Band gap extraction for the ZnO nanostructures ((A)—CBD, (B)—CNTs, (C)—CoPs, (D)—GO, (E)—HT, (F)—CNTs-GO).

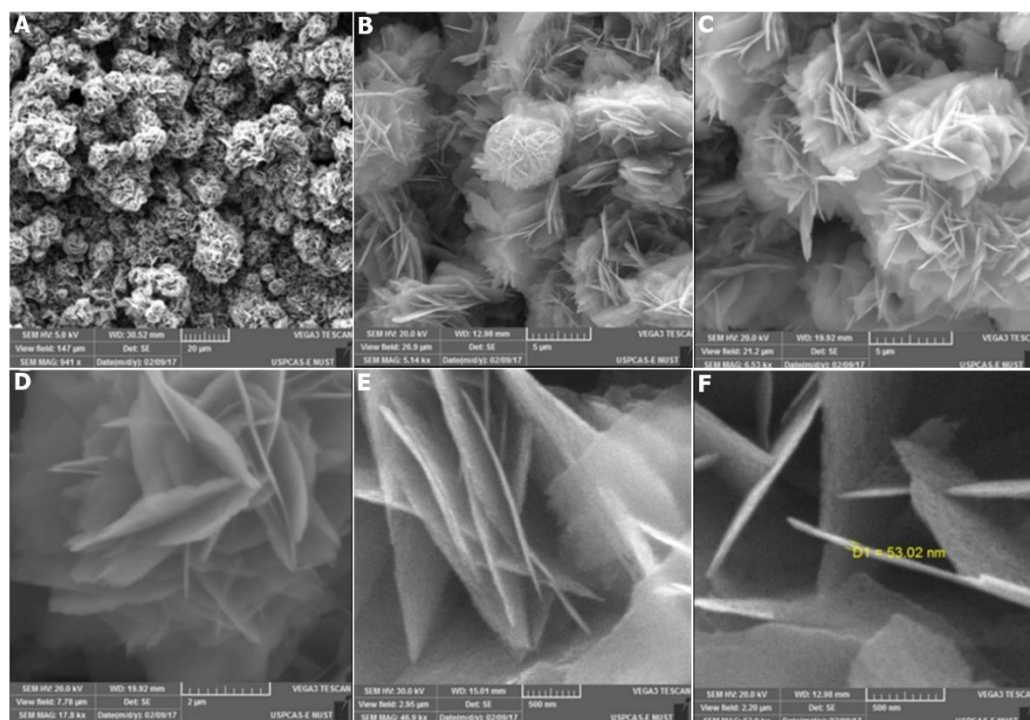


**Figure 7.** SEM images representing different magnifications of ZnO nanoflowers ((A) 20  $\mu\text{m}$ , (B,C)—5  $\mu\text{m}$ , (D) 2  $\mu\text{m}$ , (E,F)—0.5  $\mu\text{m}$ ,) grown on FTO via the hydrothermal technique.

The SEM micrographs of HT grown ZnO nanostructures in powdered form are given in Figure 8A,B with different magnifications. They reveal randomly shaped clusters of dispersed ZnO fibers with a dimension of around 1  $\mu\text{m}$  and the lower magnification has yet demonstrated the nanoflowers' arrangement.

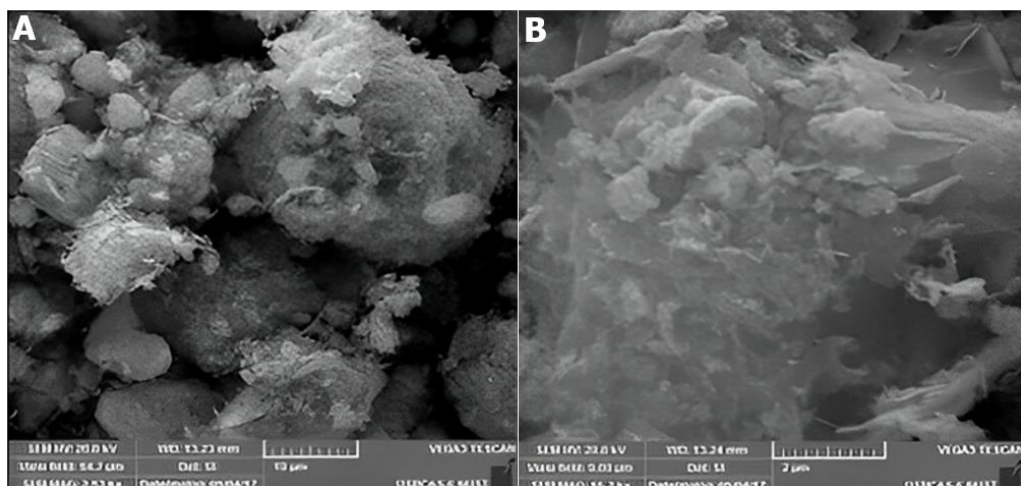


**Figure 8.** SEM images of fiber-like ZnO ((A)—10  $\mu\text{m}$ , (B)—2  $\mu\text{m}$ ) grown by hydrothermal technique.

#### 2.4.2. Morphology of ZnO Nanostructures Grown by Co-Precipitation Method

ZnO structures grown by co-precipitation method (CoP) (at 70  $^{\circ}\text{C}$ ) produced porous rhombohedral-shaped ZnO (Figure 9A,B), as confirmed by the SEM micrographs of various magnifications. The average particle size is about 1  $\mu\text{m}$ , which is further composed of randomly shaped nanoparticles and can be viewed from the higher magnified image (Figure 9B). The average length of these nanostructures is up to 400 nm.

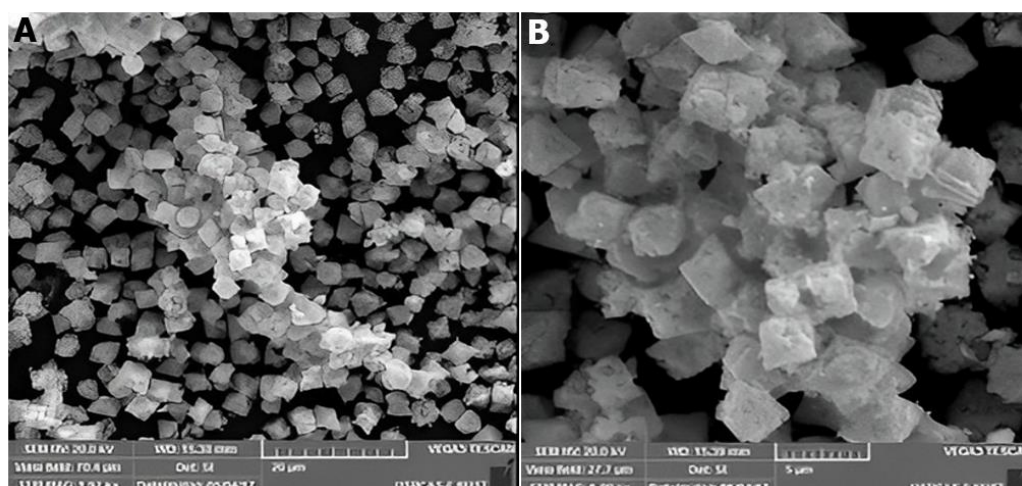


**Figure 9.** SEM images of rhombohedral ZnO nanostructures grown by the CoP method ((A)—20  $\mu\text{m}$ , (B)—5  $\mu\text{m}$ ).

#### 2.4.3. Morphology of ZnO Nanostructures Grown by Chemical Bath Deposition Method

ZnO nanostructures grown by the CBD method at 90  $^{\circ}\text{C}$  for 12 h in an oven were characterized by SEM. The SEM images of ZnO nanostructure with different magnification are given in Figure 10A,B. These micrographs show a dense assembly of ZnO NRs (having diameter in the range of 1–3  $\mu\text{m}$ ) in the form of distinct bundles which have emerged from the common origin. Thus, the CBD process has favored the formation of nanorods-like ZnO nanoparticles.

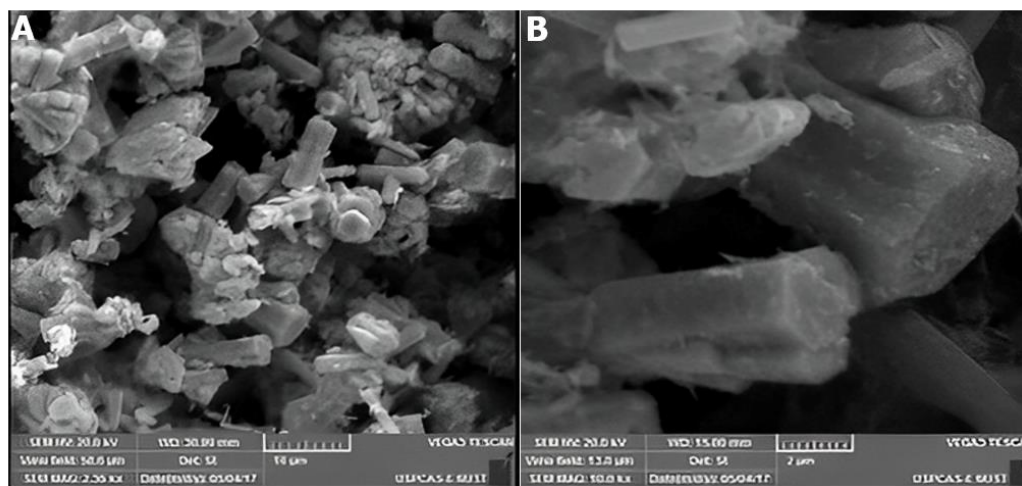


**Figure 10.** SEM images of ZnO nanorods synthesized by the CBD method ((A)—10  $\mu\text{m}$ , (B)—2  $\mu\text{m}$ ).

A variation in length, size and shape of nanorods can also be observed as only a few nanorods exhibit smooth surfaces with hexagonal symmetry at their end. Figure 11 shows the SEM image of a cauliflower-like ZnO nanostructure synthesized by the CBD method. It clearly shows that a number of ZnO NRs with hexagonal symmetry have been instigated from the common point and aggregated together to form a cauliflower-like nanostructure.

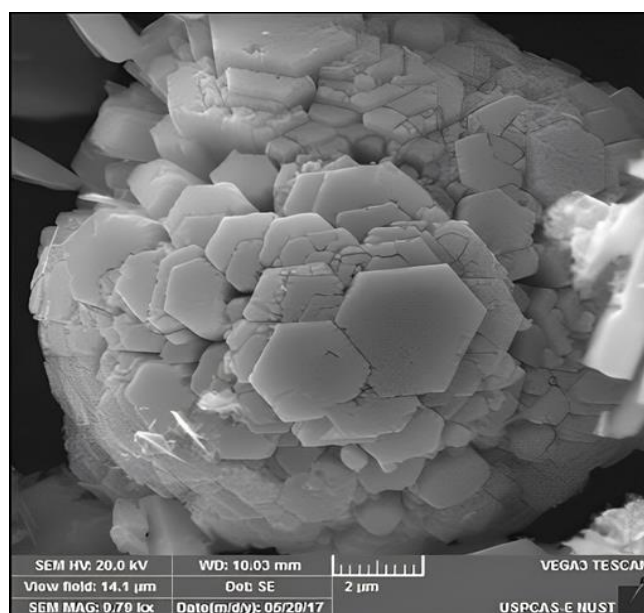


**Figure 11.** SEM micrograph of cauliflower-like ZnO nanostructures synthesized by CBD method (magnification-2  $\mu\text{m}$ ).

### 2.5. Morphology of ZnO/Carbon Nanocomposites Grown via the CBD Method

To enhance the absorbing layer performance attaining maximum light absorption and to improve the electron transport properties of ZnO, the carbon nanotubes have been incorporated into ZnO in lower percentage. For this purpose, both the materials were dispersed in solvents and mixed together to synthesize the nanocomposites.

#### 2.5.1. Morphology of ZnO/CNTs Nanocomposites

The SEM images of ZnO/CNTs nanocomposites synthesized by the CBD method by mixing 0.05 wt% MWCNTs in ZnO nanostructures are shown in Figure 12A–F. Contrary to the pure ZnO nanostructure, these images clearly show that the surface of arbitrarily aligned highly dense nanorods and hexagonal ZnO nanostructures is rough. Besides the presence of nanorods in various sizes and lengths, some ZnO nanoflakes are also visible with MWCNTs rooted on the surface of the flakes. Higher magnification reveals better connectivity of MWCNTs with ZnO. The average diameter of ZnO nanorods is observed to be in the range of 200–500 nm.

#### 2.5.2. Morphology of ZnO/Graphene Oxide Nanocomposites

The SEM images of ZnO/GO nanocomposites formed by adding 0.05 wt% GO in ZnO nanomaterial grown by the CBD method are represented in Figure 13A–F. The images show randomly oriented small-sized individual as well as bundled ZnO nanorods distributed at the surface. The sheet-like arrangement on the surface of nanostructures visible at higher magnification indicates the dispersion of graphene due to the hydrophilic groups at its surface, but cannot be easily identified because of the small percentage.

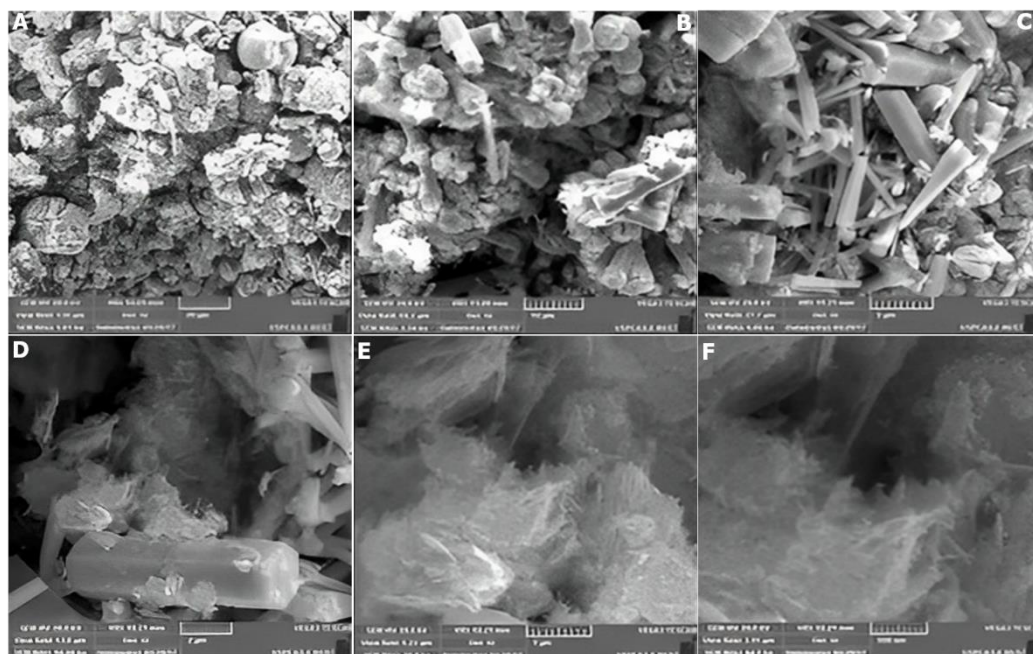


**Figure 12.** SEM images of ZnO/CNTs nanocomposites synthesized by the CBD method ((A)—20  $\mu\text{m}$ , (B)—10  $\mu\text{m}$ , (C)—5  $\mu\text{m}$ , (D)—2  $\mu\text{m}$ , (E)—1  $\mu\text{m}$ , (F)—0.5  $\mu\text{m}$ ).

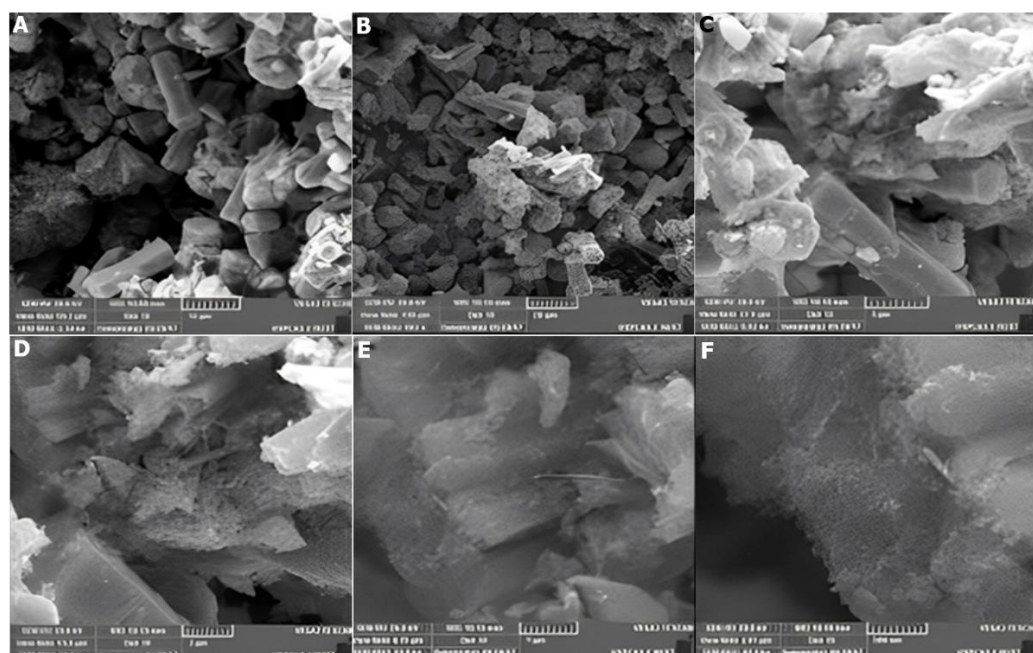


**Figure 13.** SEM images of ZnO/GO nanocomposite grown by the CBD method (A)—10  $\mu\text{m}$ , (B)—20  $\mu\text{m}$ , (C)—5  $\mu\text{m}$ , (D)—2  $\mu\text{m}$ , (E)—1  $\mu\text{m}$ , (F)—0.5  $\mu\text{m}$ .

### 2.5.3. Morphology of ZnO/CNTs/GO Nanocomposites

The SEM images of the composite of ZnO/CNTs/GO, synthesized by mixing ZnO powder with 0.05 wt.% GO and 0.05 wt.% are given in Figure 14A–D. The micrographs reveal a compact high surface roughness which has few individually present ZnO nanorods with hexagonal symmetry and others aligned together in the cauliflower-shape originated from the common origin with embedded MWCNTs and GO. The average diameter of ZnO nanostructures was found to be 500 nm.

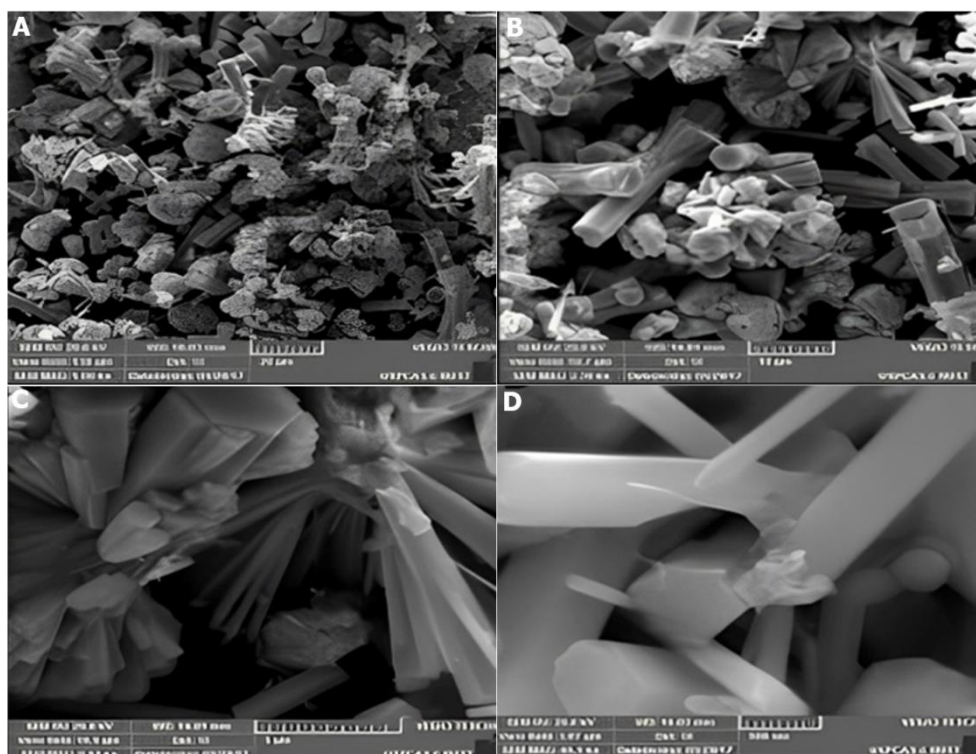


**Figure 14.** SEM images of ZnO-CNTs + GO nanocomposites: (A)—20  $\mu\text{m}$ , (B)—10  $\mu\text{m}$ , (C)—5  $\mu\text{m}$ , and (D)—0.5  $\mu\text{m}$ .

## 2.6. Energy Dispersive X-ray Spectroscopic (EDX) Analysis

Energy dispersive X-ray (EDX) analyses of the samples prepared through different techniques, i.e., HT, CoP and CBD were performed for investigating the elemental composition of the synthesized nanostructures and nanocomposites.

### 2.6.1. EDX Analysis of ZnO Nanostructures

The EDX analysis confirms the elemental composition of the synthesized nanomaterials. The EDX spectra of pristine ZnO grown by HT, CoP and CBD techniques are presented in Figure 15A–C. The figure shows that the nanostructures synthesized by all these methods are comprised only zinc (Zn) and oxygen (O) elements and no impurities are present.

### 2.6.2. EDX Analysis of ZnO/CNTs/GO Nanocomposites

The presence of carbon in the nanocomposites ZnO/GO, ZnO/CNTs, and ZnO/CNTs/GO grown by CBD technique was confirmed from the elemental analysis using EDX. The spectra presented in Figure 16 evidently show the presence of elemental carbon with a higher atomic concentration, which indicates the inclusion of GO and CNTs into the ZnO nanostructure.

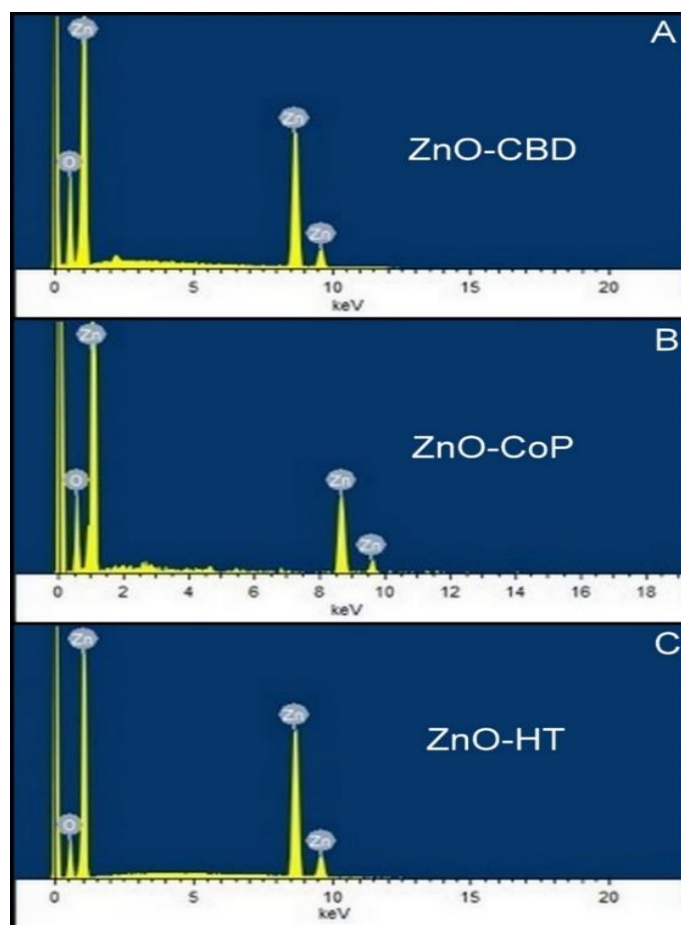


**Figure 15.** EDX spectra of ZnO grown via the HT, CoP and CBD methods ((A)—CBD, (B)—CoP, (C)—HT).

### 2.7. Current-Density Voltage Analysis of ZnO Based Dye Sensitized Solar Cells

The dye sensitized solar cell (DSSC) was assembled using ZnO as the photoanode, N719 as the dye, iodide/triiodide as the electrolyte and platinum as the counter electrode. The power conversion efficiency (PCE) of the fabricated DSSCs was calculated using current density-voltage (J-V) curves and was measured under AM 1.5G illumination. The J-V characteristics of Zinc Oxide synthesized by different techniques are given in Figure 17. It can be seen from the figure that the ZnO synthesized by hydrothermal process with the nanoflower morphology having the best results with the  $V_{oc}$  as 0.513 V, the  $J_{sc}$  as  $4.82 \text{ mA/cm}^2$  and Fill Factor (FF) as 0.59. The maximum current density led to an improved conversion efficiency of 1.45% which overcomes the small reduction in  $V_{oc}$ . The  $J_{sc}$  varies with the surface area of the nanoparticles, hence, nanoflowers with an increased surface area can assimilate more dye and this results profound  $J_{sc}$  and thus greater efficiency. However, the DSSC based on ZnO grown by CBD with nanorods morphology achieved the  $V_{oc}$  as 0.407 V, the  $J_{sc}$  as  $4.42 \text{ mA/cm}^2$  and the FF as 0.63. The nanorods' morphology has exhibited higher  $J_{sc}$  probably by providing \ direct path to photogenerated electrons with a power conversion efficiency of 1.14%. The ZnO grown by CoP with a cuboid and rhombohedral structure exhibited lower efficiency of 1.12% with  $V_{oc}$ ,  $J_{sc}$  and FF values of 0.568 V,  $3.34 \text{ mA/cm}^2$  and 0.59, respectively.

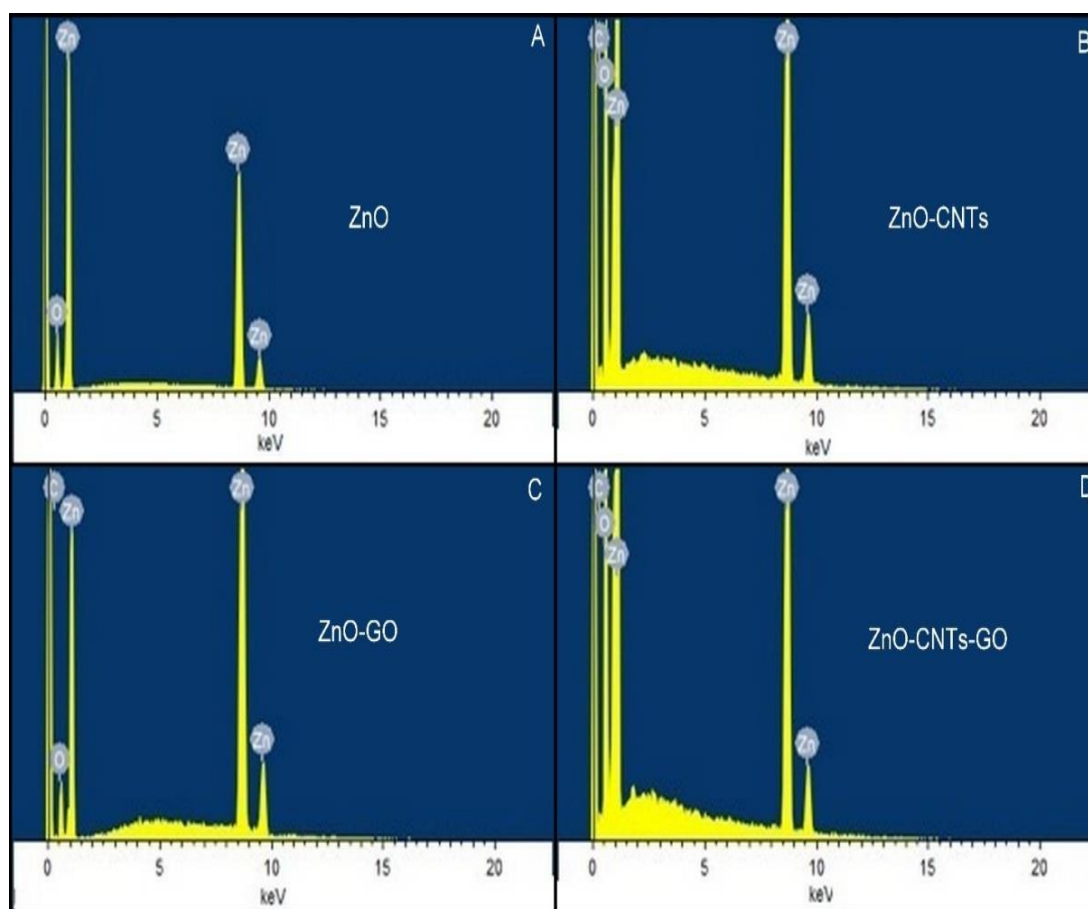


**Figure 16.** EDX spectra of ZnO/CNTs/GO non-material grown via the the CBD method ((A)—ZnO, (B)—CNTs, (C)—GO, (D)—CNTs-Go).

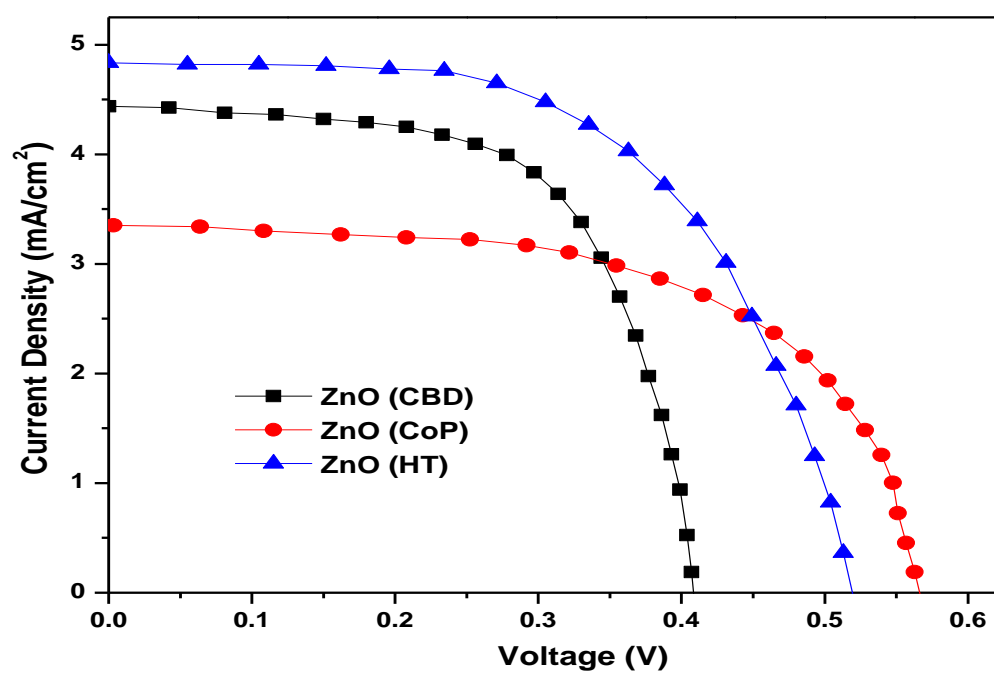


**Figure 17.** J-V plot of ZnO nanostructures grown through different techniques.

The J-V characteristics of pure ZnO and its nanocomposites with carbon, prepared through CBD, are shown in Figure 18. It can be observed that the ZnO/CNTs nanocomposite exhibits the maximum conversion efficiency, i.e., 1.23%, and the other reflective electrical parameters, the  $V_{oc}$ ,  $J_{sc}$  and FF, are observed as 0.422 V, 4.49 mA/cm<sup>2</sup> and 0.65, respectively. The increased efficiency can be credited to the effective mixing of CNTs into ZnO nanostructures, which encourages the fast transport of photon-generated electrons by providing conductive paths between the ZnO nanorods and therefore leads to a higher  $J_{sc}$ . The ZnO/GO/CNTs nanocomposite gave an efficiency of 0.86%, the  $V_{oc}$  as 0.412 V, the  $J_{sc}$  as 3.45 mA/cm<sup>2</sup> and the FF as 0.61. However, the ZnO/GO showed minimum conversion efficiency of 0.77% with  $J_{sc}$ ,  $V_{oc}$  and FF values as 2.67 mA/cm<sup>2</sup>, 0.451 V and 0.64, respectively.

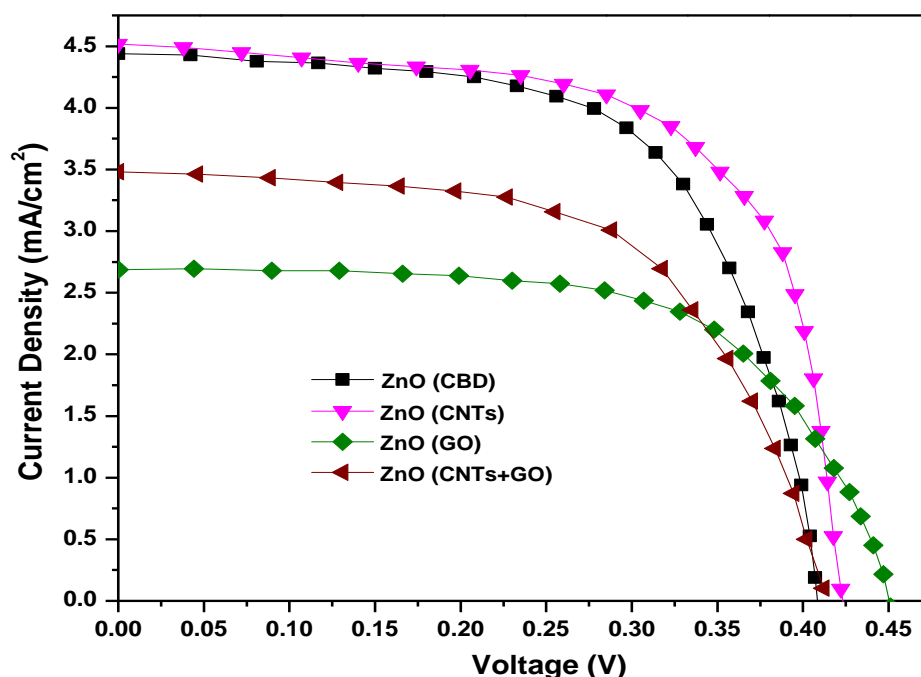


Figure 18. Electrical characteristics of ZnO nanostructures and ZnO nanocomposites with carbon.

Lower efficiency in the case of ZnO/GO can be related to the reduced conductivity of graphene oxide due to deficient pi conjugation, i.e., lower than a micro-S/m with a C/O ratio of 2/1. Hence, converting the GO to RGO produces better conductivity values which further helps in the improved efficiency of the DSC. The electrical behavior of the synthesized nanostructures and nanocomposites are given in Table 3.

Table 3. Electrical parameters of DSCs.

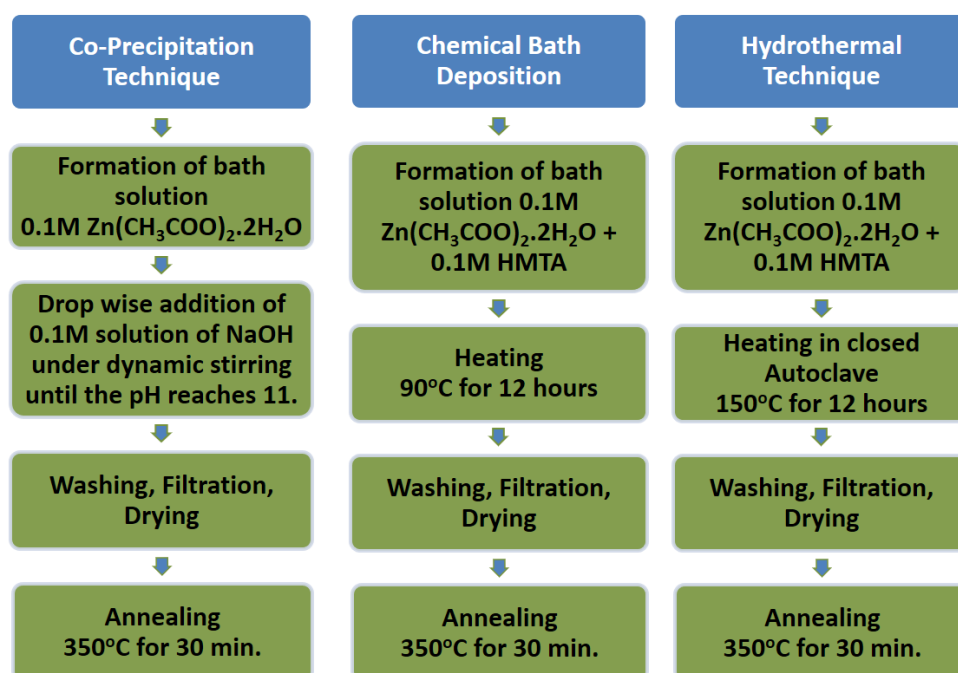
Samples	$V_{oc}$ (V)	$J_{sc}$ (mA/cm <sup>2</sup> )	$V_{mp}$ (V)	$J_{mp}$ (mA/cm <sup>2</sup> )	FF	$\eta$ (%)
ZnO (HT)	0.513	4.89	0.363	4.02	0.59	1.99
ZnO (CoP)	0.568	3.34	0.415	2.17	0.59	1.50
ZnO (CBD)	0.407	4.42	0.314	3.63	0.63	1.52
ZnO (CNTs)	0.422	4.49	0.322	3.85	0.65	1.66
ZnO (GO)	0.451	2.67	0.328	2.34	0.64	1.02
ZnO (CNTs + GO)	0.412	3.45	0.317	2.74	0.61	1.16

Various attempts have been made to enhance the efficiency of DSSCs by using ZnO-CNTs composites as photoanodes [42–44]. The addition of CNMs in ZnO photo anodes provides another conduction route for electronic transport, which decreases the resistance between electrolyte/electrode, reducing the recombination losses and thus constructing a remarkable and unique path for DSSCs. It is observed that blending of ZnO and CNTs in the form of nanocomposite thin film possessed enhanced electrical conductance in the DSSC, possibly by offering a higher specific surface area leading to improved dye adsorption [44–48]. The CNTs assist in electrolyte/electrode interfacial barrier reduction which consequently results into smaller recombination and enhancement of ZnO interconnectivity [49]. For instance, Tumcharern et al. [43] studied the impact of MWCNTs' incorporation in the ZnO photoanode. J-V characteristics of ZnO-MWCNTs photoanode revealed that 0.05 wt.% MWCNTs possessed a 42% improved conversion efficiency of 0.77% in comparison to that of pure ZnO photoanode and a 32% enhanced  $J_{sc}$  of  $2.33 \text{ mA cm}^{-2}$ ,  $V_{oc}$  of 0.62 V, FF of 0.53%. At 0.3 wt.% MWCNT, ZnO/MWCNT composite displayed enhanced  $J_{sc}$  of  $11.85 \text{ mA/cm}^2$ ,  $V_{oc}$  of 0.48 V, FF of 48.76% and greater conversion efficiency of 2.77% than that of the pure ZnO cell (2.37%).

### 3. Experimental

#### 3.1. Materials and Synthesis Methods

Multi-walled CNTs (NC3101) with 95% purity and -COOH functionalized for about >8% were purchased from NANOCYL. The average length of these carbon nanotubes (CNTs) was  $1.5 \mu\text{m}$  and the average diameter was 9.5 nm. Graphene oxide was purchased from CHEAPTUBES. Analytical grade materials, i.e., Zinc acetate dihydrate [ $\text{Zn}(\text{CH}_3\text{COO})_2 \cdot 2\text{H}_2\text{O}$ ,  $\geq 99.0\%$ ], Zinc Nitrate hexahydrate [ $\text{Zn}(\text{NO}_3)_2 \cdot 6\text{H}_2\text{O}$ ,  $\geq 99.0\%$ ], hexamethylenetetramine (HMTA) [ $\text{C}_6\text{H}_{12}\text{N}_4$ ,  $\geq 99.0\%$ ], Fluorine-doped tin oxide [ $\text{F:SnO}_2$ ,  $22 \Omega/\text{cm}^2$ ]-coated glasses, N719 dye [Ruthenizer 535bis-TBA] electrolyte [Iodolyte AN50] and absolute ethanol [ $\text{CH}_3\text{CH}_2\text{O}$ , 99.8%], were purchased from Sigma Aldrich and distilled water was used. All the chemicals were used as received without further purification. ZnO was synthesized by using various techniques as depicted in Scheme 1.



**Scheme 1.** Schematic representation for the synthesis of ZnO via various techniques.

### 3.2. Film Fabrication

For film fabrication, two methods have been used which include direct growth on FTO and film deposition by the doctor-blade technique. For direct growth onto FTO substrate, a hydrothermal method or CBD was used. A substrate holder was used to hold and fix the FTO substrate. The FTO substrate's conducting side was in downward position to prevent the precipitates from dropping onto the glass substrate from the solution. Then, the arrangement was positioned in a vertical direction in the prepared solution. For the hydrothermal technique, an autoclave or a beaker for the CBD process were used. Afterwards, to avoid the ammonia volatilization, the autoclave/beaker was sealed and placed in an oven at 120 °C for 18 h. Then, the substrate with a thick, white film layer was removed from the solution, washed with deionized water and then dried. Doctor-blade printing is the simplest technique for the current electronics technology, so it was used for ZnO films fabrication. This method is similar to tape casting and most appropriate for thick films fabrication. For uniform dispersion of the prepared paste on the FTO substrate surface to form stable, thick film, a blade was used as indicated by its name. This is a cost-effective technique, as the 5% particles loss is reduced as compared to the spin coating method [50]. For the mixed solvent paste synthesis, 1 vol% acetic acid, 32 vol% deionized water, and 67 vol% ethanol was used. Afterward, dispersion of ZnO particles in paste solution with a 1:2 weight ratio of ZnO and paste solution was carried out. Then, constant stirring was maintained until the formation of a colloidal suspension and then ultrasonication was carried out for 4 h. The paste obtained in a circular shape was deposited via doctor-blading on the FTO substrate and film explicit parts which were not used for growth were covered by Teflon tape. The covered films were dried at 90 °C for 30 min and then annealed at 350 °C in a furnace to form thin smooth films photoanode.

### 3.3. Cell Fabrication

The top surface of DSSCs is an anode which is transparent and made up of glass plates with FTO deposited on the backside. On the back of conductive plate, there is a thin layer of semiconducting metal oxide, which has a high specific area, and is extremely porous and chemically bounded by sintering. The plate with two sides, an anode with SnO<sub>2</sub>: F coated side and a conductive side, is soaked in a mixture which consists of a solvent and a dye (N719), and this is the photosensitive part of DSCs [51,52]. This dipping in the mixture forms a very thin layer of the dye on the semiconducting oxide surface. It is bonded covalently and this may be through a bidentate bridging association or through a chelating ester. The arrangement of counter electrodes includes an iodide/triiodide electrolyte which is extended over a platinum sheet. The platinum sheet is conductive and acts as a catalyst. Then, a connection is made between the two plates and the cell is then sealed to avoid any electrolyte leakage [53].

To fabricate the microfluidic DSCs, the first step was the immersion of photoanodes in a dye solution at room temperature for an optimized time interval and then washing them with solvent to eliminate any weakly attached non-adherent dye molecules. To develop an inlet and outlet connections, two small pin holes were used for counter electrodes and FTO substrates via a powder-blasting method. Then, rinsing of FTO glasses was done. First, the FTO glasses were dipped in acetone, then ultrasonicated for about 10 min and then bathing with isopropanol was done. Afterwards, a 1:3 piranha solution of hydrogen peroxide: sulfuric acid was prepared and then the FTO glasses were dipped in this solution for about 10 min. The glasses were then washed with deionized water to remove organic scums and then a nitrogen shower was employed for drying. For deposition of the 5 nm platinum layer on the FTO glass, thermal evaporation was used. For the operating chamber, the PDMS membrane (200 ± 15 µm) was synthesized by a casting method. The PDMS (polydimethylsiloxane) membrane literally defines the active chamber of the cell. A design with double drop membrane was used to elevate air bubble removal from the process of filling the electrolyte. Furthermore, sealing of the cells was carried out by using external housing systems which consist of PMMA (Poly Methyl Meth

Acrylate) frame structures which aid in the fixing of the two electrodes and also allow the control and management of fluids. A syringe, which is attached to PDMS O-ring interconnections (housing ports) by means of LDPE (low-density polyethylene) tubes was used for the filling electrolyte. Lastly, wrapping of ports by using homemade caps was carried out. Home-made caps consisted of low-density polyethylene tubes which were filled with PDMS. This process and arrangement are flexible because they allow control and examination after performing experiments. The active area of all the cells was measured and equal to  $0.78 \text{ cm}^2$  approximately and these measurements were carried out by using a shadow mask area of  $0.22 \text{ cm}^2$ . Copper foils of a  $50 \text{ }\mu\text{m}$  thickness and  $1.5 \text{ cm}^2$  area were used for the electrical connection of electrodes. PDMS membranes were used between the electrodes which act as a dielectric between the electrodes. Electrical connections at the electrodes, which are dielectrically separated by means of PDMS membranes, were made by using  $50 \text{ }\mu\text{m}$  thick copper foils with an area of  $1.5 \text{ cm}^2$ .

### 3.4. Characterization

ZnO thin films were characterized through various physicochemical techniques for investigating the nature of material, surface roughness, band gap and transparency. The crystal structure of the sample was investigated using X-ray diffraction (XRD; Bruker D8 Advance, X-ray diffractometer) with CuK $\alpha$  radiation at a scan rate of  $4 \text{ min}^{-1}$ . The acceleration voltage and applied current were 40 kV and 40 mA, respectively. The samples' morphology was examined using a field emission scanning electronic microscope (FESEM, FEI Quanta 200 F; accelerating voltage = 10 kV). A Shimadzu UV-4100 spectrophotometer was used to perform UV-Vis diffuse reflection spectroscopy (DRS) with BaSO $_4$  as the reference material.

## 4. Conclusions

Different ZnO-based photoanodes exhibiting various morphologies have been successfully fabricated and employed in the DSCs preparation. It was found that the ZnO photoanode with nanoflower morphology exhibits enough specific surface area for efficient dye adsorption. Thus, it offers effective conduction paths owing to interlinked networks thus causing it to enhance the  $J_{\text{SC}}$ . It is observed that the optical absorbance of nanocomposites was improved by the addition of GO and CNTs into the ZnO nanostructure. The electrical characterization of DSCs revealed that the ZnO nanocomposite with CNTs exhibited a higher power conversion efficiency of 1.23%, which can be attributed to the higher conductivity of CNTs because it provides a one-dimensional pathway to the photon-generated electrons. However, the addition of GO has not effectively changed the performance of DSC. The main reason for its lower  $J_{\text{SC}}$  value could be due to lower conductivity of the GO resulting in poor electron transport and thus lower efficiency.

**Author Contributions:** H.G.'s contribution in this article is conceptualization, overall supervision, and review and editing of the manuscript. N.F. carried out the experimental work and wrote the first draft of the paper. N.S. and M.I.S. provided facilities for the formal analysis. M.S., M.H. (Muhammad Hussain) and M.H. (Muhammad Humayun) contributed to the review and editing of the article. All authors have read and agreed to the published version of the manuscript.

**Funding:** This research received no external funding.

**Acknowledgments:** The authors are thankful to the administration of National Center for Physics, Islamabad for providing lab facilities.

**Conflicts of Interest:** The authors declare no conflict of interest.

## References

- Lee, T.H.; Sue, H.J.; Cheng, X. Solid-state dye-sensitized solar cells based on ZnO nanoparticle and nanorod array hybrid photoanodes. *Nanoscale Res. Lett.* **2011**, *6*, 517. [\[CrossRef\]](#) [\[PubMed\]](#)
- Barber, G.D.; Hoertz, P.G.; Lee, S.-H.A.; Abrams, N.M.; Mikulca, J.; Mallouk, T.E.; Liska, P.; Zakeeruddin, S.M.; Gratzel, M.; Ho-Baillie, A.; et al. Utilization of Direct and Diffuse Sunlight in a Dye-Sensitized Solar Cell—Silicon Photovoltaic Hybrid Concentrator System. *J. Phys. Chem. Lett.* **2011**, *2*, 581–585. [\[CrossRef\]](#)
- Klaus, J.; Isabella, O.; Smets, A.H.M.; Swaaij, R.A.C.M.M.; Zeman, M. *Solar Energy Fundamentals, Technology, and Systems*; Delft University of Technology: Delft, The Netherlands, 2014.
- O'Regan, B.; Gratzel, M. A low-cost, high-efficiency solar cell based on dye-sensitized colloidal TiO<sub>2</sub> films. *Nature* **1991**, *353*, 737–740. [\[CrossRef\]](#)
- Grätzel, M. Dye-sensitized solar cells. *J. Photochem. Photobiol. C Photochem. Rev.* **2003**, *4*, 145–153. [\[CrossRef\]](#)
- Al, N.; Hussain, A.; Ahmed, R.; Wang, M.K.; Zhao, C.; Haq, B.U.; Fu, Y.Q. Advances in nanostructured thin film materials for solar cell applications. *Renew. Sustain. Energy Rev.* **2016**, *59*, 726–737. [\[CrossRef\]](#)
- Albero, J.; Atienzar, P.; Corma, A.; Garcia, H. Efficiency Records in Mesoscopic Dye-Sensitized Solar Cells. *Chem. Rec.* **2015**, *15*, 803–828. [\[CrossRef\]](#) [\[PubMed\]](#)
- Liu, X.; Fang, J.; Liu, Y.; Lin, T. Progress in nanostructured photoanodes for dye-sensitized solar cells. *Front. Mater. Sci.* **2016**, *10*, 225–237. [\[CrossRef\]](#)
- Memarian, N.; Concina, I.; Braga, A.; Rozati, S.M.; Vomiero, A.; Sberveglieri, G. Hierarchically Assembled ZnO Nanocrystallites for High-Efficiency Dye-Sensitized Solar Cells. *Angew. Chem. Int. Ed.* **2011**, *50*, 12321–12325. [\[CrossRef\]](#)
- Martinson, A.B.F.; Elam, J.W.; Hupp, J.T.; Pellin, M.J. ZnO Nanotube Based Dye-Sensitized Solar Cells. *Nano Lett.* **2007**, *7*, 2183–2187. [\[CrossRef\]](#)
- Martinson, A.B.F.; McGarrah, J.E.; Parpia, M.O.K.; Hupp, J.T. Dynamics of charge transport and recombination in ZnO nanorod array dye-sensitized solar cells. *Phys. Chem. Chem. Phys.* **2006**, *8*, 4655–4659. [\[CrossRef\]](#)
- Qiu, Y.; Yang, S. ZnO Nanotetrapods: Controlled Vapor-Phase Synthesis and Application for Humidity Sensing. *Adv. Funct. Mater.* **2007**, *17*, 1345–1352. [\[CrossRef\]](#)
- Zhang, W.; Wang, P.; Fei, X.; Xiu, Y.; Jia, G. Growth Mechanism and Morphologies Tuning of ZnO Nanostructures. *Int. J. Electrochem. Sci.* **2015**, *10*, 4688–4695.
- Zhang, Q.; Dandeneau, C.S.; Zhou, X.; Cao, G. ZnO Nanostructures for Dye-Sensitized Solar Cells. *Adv. Mater.* **2009**, *21*, 4087–4108. [\[CrossRef\]](#)
- Wang, Z.L. Zinc oxide nanostructures: Growth, properties and applications. *J. Phys. Condens. Matter* **2004**, *16*, R829–R858. [\[CrossRef\]](#)
- Tyona, M.D.; Osuji, R.U.; Ezema, F.I. A review of zinc oxide photoanode films for dye-sensitized solar cells based on zinc oxide nanostructures. *Adv. Nano Res.* **2013**, *1*, 43–58. [\[CrossRef\]](#)
- Yun, Y.S.; Park, J.Y.; Oh, H.; Kim, J.J.; Kim, S.S. Electrical transport properties of size-tuned ZnO nanorods. *J. Mater. Res.* **2006**, *21*, 132–136. [\[CrossRef\]](#)
- Yi, G.C.; Wang, C.; Park, W.I. ZnO nanorods: Synthesis, characterization and applications. *Semicond. Sci. Technol.* **2005**, *20*, S22–S34. [\[CrossRef\]](#)
- Kong, X.Y.; Wang, Z.L. Spontaneous Polarization-Induced Nanohelices, Nanosprings, and Nanorings of Piezoelectric Nanobelts. *Nano Lett.* **2003**, *3*, 1625–1631. [\[CrossRef\]](#)
- Kong, X.Y.; Ding, Y.; Yang, R.; Wang, Z.L. Single-Crystal Nanorings Formed by Epitaxial Self-Coiling of Polar Nanobelts. *Science* **2004**, *303*, 1348–1351. [\[CrossRef\]](#)
- Wang, J.S.; Yang, C.S.; Chen, P.I.; Su, C.F.; Chen, W.J.; Chiu, K.C.; Chou, W.C. Catalyst-free highly vertically aligned ZnO nanoneedle arrays grown by plasma-assisted molecular beam epitaxy. *Appl. Phys. A* **2009**, *97*, 553–557. [\[CrossRef\]](#)
- Wahab, R.; Ansari, S.G.; Kim, Y.S.; Seo, H.K.; Shin, H.S. Room temperature synthesis of needle-shaped ZnO nanorods via sonochemical method. *Appl. Surf. Sci.* **2007**, *253*, 7622–7626. [\[CrossRef\]](#)
- Satoh, Y.; Ohshio, S.; Saitoh, H. Photoluminescence spectroscopy of highly oriented Y<sub>2</sub>O<sub>3</sub>: Tb crystalline whiskers. *Sci. Technol. Adv. Mater.* **2016**, *6*, 215–218. [\[CrossRef\]](#)
- Hu, J.Q.; Bando, Y. Growth and optical properties of single-crystal tubular ZnO whiskers. *Appl. Phys. Lett.* **2003**, *82*, 1401–1403. [\[CrossRef\]](#)
- Gao, P.X.; Wang, Z.L. Mesoporous Polyhedral Cages and Shells Formed by Textured Self-Assembly of ZnO Nanocrystals. *J. Am. Chem. Soc.* **2003**, *125*, 11299–11305. [\[CrossRef\]](#) [\[PubMed\]](#)
- Ding, G.Q.; Shen, W.Z.; Zheng, M.J.; Fan, D.H. Synthesis of ordered large-scale ZnO nanopore arrays. *Appl. Phys. Lett.* **2006**, *88*, 103106. [\[CrossRef\]](#)
- Wan, Q.; Wang, T.H.; Zhao, J.C. Enhanced photocatalytic activity of ZnO nanotetrapods. *Appl. Phys. Lett.* **2005**, *87*, 083105. [\[CrossRef\]](#)
- Gao, P.X.; Wang, Z.L. Nanopropeller arrays of zinc oxide. *Appl. Phys. Lett.* **2004**, *84*, 2883–2885. [\[CrossRef\]](#)
- Yang, P.; Yan, H.; Mao, S.; Russo, R.; Johnson, J.; Saykally, R.; Morris, N.; Pham, J.; He, R.; Choi, H.J. Controlled Growth of ZnO Nanowires and Their Optical Properties. *Adv. Funct. Mater.* **2002**, *12*, 323–331. [\[CrossRef\]](#)
- Wang, Z.L. Novel Zinc Oxide Nanostructures Discovery by Electron Microscopy. *J. Phys. Conf. Ser.* **2006**, *26*, 1–6. [\[CrossRef\]](#)

31. Xu, C.X.; Sun, X.W. Field emission from zinc oxide nanopins. *Appl. Phys. Lett.* **2003**, *83*, 3806–3808. [[CrossRef](#)]
32. Lao, J.Y.; Haung, J.Y.; Ren, Z.F. ZnO Nanobridges and Nanonails. *Nano Lett.* **2003**, *3*, 235–238. [[CrossRef](#)]
33. Lao, C.S.; Shi, L.C.; Gao, P.X.; Sen, Y.R.; Yue, Z.; Ying, D.; Wang, Z.L. Formation of double-side teathed nanocombs of ZnO and self-catalysis of Zn-terminated polar surface. *Chem. Phys. Lett.* **2006**, *417*, 358–362. [[CrossRef](#)]
34. Yang, Z.; Xu, T.; Ito, Y.; Welp, U.; Kwok, W.K. Enhanced Electron Transport in Dye-Sensitized Solar Cells Using Short ZnO Nanotips on A Rough Metal Anode. *J. Phys. Chem. C* **2009**, *113*, 20521–20526. [[CrossRef](#)]
35. Xu, C.X.; Xu, C.X.; Sun, X.W.; Dong, Z.L.; Yu, M.B. Zinc oxide nanodisk. *Appl. Phys. Lett.* **2004**, *85*, 3878–3880. [[CrossRef](#)]
36. Hu, J.Q.; Li, Q.; Meng, X.M.; Lee, C.S.; Lee, S.T. Thermal Reduction Route to the Fabrication of Coaxial Zn/ZnO Nanocables and ZnO Nanotubes. *Chem. Mater.* **2003**, *15*, 305–308. [[CrossRef](#)]
37. Hu, J.Q.; Bando, Y.; Zhan, J.H.; Li, Y.B.; Sekiguchi, T. Two-dimensional micrometer-sized single-crystalline ZnO thin nanosheets. *Appl. Phys. Lett.* **2003**, *83*, 4414. [[CrossRef](#)]
38. Jiang, C.Y.; Sun, X.W.; Lo, G.Q.; Kwong, D.L. Improved dye-sensitized solar cells with a ZnO-nanoflower photoanode. *Appl. Phys. Lett.* **2007**, *90*, 263501. [[CrossRef](#)]
39. Abdullah, H.; Ariyanto, N.P.; Shaari, S.; Yulianto, B.; Junaidi, S. Study of porous nanoflake ZnO for dye-sensitized solar cell application. *Am. J. Eng. Appl. Sci.* **2009**, *2*, 236–240.
40. Radzimska, A.K.; Jesionowski, T. Zinc Oxide-From Synthesis to Application: A Review. *Materials* **2014**, *7*, 2833–2881. [[CrossRef](#)]
41. Wu, C.-T.; Liao, W.-P.; Wu, J.-J. Three-dimensional ZnO nanodendrite/nanoparticle composite solar cells. *J. Mater. Chem.* **2011**, *21*, 2871–2876. [[CrossRef](#)]
42. Chang, W.-C.; Cheng, Y.Y.; Yu, W.C.; Yao, Y.C.; Lee, C.H.; Ko, H.H. Enhancing performance of ZnO dye-sensitized solar cells by incorporation of multiwalled carbon nanotubes. *Nanoscale Res. Lett.* **2012**, *7*, 166. [[CrossRef](#)] [[PubMed](#)]
43. Chindaduang, A.; Duangkaew, P.; Pratontep, S.; Tumcharern, G. Effects of Multi-walled Carbon Nanotube Incorporation in ZnO Photoelectrode on the Efficiency of Dye-Sensitized Solar Cells. *NU Sci. J.* **2009**, *6*, 28–35.
44. Chindaduang, A.; Duangkaew, P.; Pratontep, S.; Tumcharern, G. Structural, Optical and Photovoltaic Properties of ZnO-MWCNTs Electrodes. *J. Microsc. Soc. Thai.* **2009**, *23*, 115–118.
45. Dai, L.; Chang, D.W.; Baek, J.B.; Lu, W. Carbon nanomaterials for advanced energy conversion and storage. *Small* **2012**, *8*, 1130–1166. [[CrossRef](#)] [[PubMed](#)]
46. Zhu, H.; Wei, J.; Wang, K.; Wu, A. Applications of carbon materials in photovoltaic solar cells. *Sol. Energy Mater. Sol. Cells* **2009**, *93*, 1461–1470. [[CrossRef](#)]
47. Ghai, P.; Kesarwani, A.; Kansal, S. Carbon Nanotubes in Photovoltaics. *Int. Adv. Res. J. Sci. Eng. Technol.* **2015**, *2*, 125–128.
48. Yen, C.Y.; Lin, Y.F.; Liao, S.H.; Weng, C.C.; Huang, C.C.; Hsiao, Y.H.; Ma, C.C.M.; Chang, M.C.; Shao, H.; Tsai, M.C.; et al. Preparation and properties of a carbon nanotube-based nanocomposite photoanode for dye-sensitized solar cells. *Nanotechnology* **2008**, *19*, 375305. [[CrossRef](#)]
49. Ramar, A.; Soundappan, T.; Chen, S.M.; Rajkumar, M.; Ramiah, S. Incorporation of Multi-Walled Carbon Nanotubes in ZnO for Dye Sensitized Solar Cells. *Int. J. Electrochem. Sci.* **2012**, *7*, 11734–11744.
50. Saito, M.; Fujihara, S. Fabrication and photovoltaic properties of dye-sensitized ZnO thick films by a facile doctor-blade printing method using nanocrystalline pastes. *J. Ceram. Soc. Japan.* **2009**, *117*, 823–827. [[CrossRef](#)]
51. Wu, J.J.; Chen, G.R.; Yang, H.H.; Ku, C.H.; Lai, J.Y. Effects of dye adsorption on the electron transport properties in ZnO-nanowire dye-sensitized solar cells. *Appl. Phys. Lett.* **2007**, *90*, 213109. [[CrossRef](#)]
52. Keis, K.; Jan Lindgren, J.; Lindquist, S.E.; Hagfeldt, A. Studies of the Adsorption Process of Ru Complexes in Nanoporous ZnO Electrodes. *Langmuir* **2000**, *16*, 4688–4694. [[CrossRef](#)]
53. Lamberti, A.; Sacco, A.; Bianco, S.; Giuri, E.; Quaglio, M.; Chiodoni, A.; Tresso, E. Microfluidic sealing and housing system for innovative dye-sensitized solar cell architecture. *Microelectron. Eng.* **2011**, *88*, 2308–2310. [[CrossRef](#)]